

---

# Rate–Distortion Signatures of Generalization and Information Trade-off in Humans and Deep Vision Models

---

Leyla Roksan Caglar<sup>1</sup> Pedro A.M. Mediano<sup>2</sup> Baihan Lin<sup>1,3,4,5</sup>

## Abstract

Generalization to novel visual conditions remains a central challenge for both human and machine vision, yet standard robustness metrics offer limited insight into how systems trade accuracy for robustness. We introduce a rate–distortion–theoretic framework that treats stimulus–response behavior as an effective communication channel, derives rate–distortion (RD) frontiers from confusion matrices, and summarizes each system with two interpretable geometric signatures - slope ( $\beta$ ) and curvature ( $\kappa$ ) - which capture the marginal cost and abruptness of accuracy–robustness trade-offs. Applying this framework to human psychophysics and 18 deep vision models under controlled image perturbations, we compare generalization geometry along model architectures and training regimes. We find that both biological and artificial systems follow a common lossy-compression principle but occupy systematically different regions of RD space. In particular, humans exhibit smoother, more flexible trade-offs, whereas modern deep networks operate in steeper and more brittle regimes even at matched accuracy. Across training regimes, robustness training induces systematic but dissociable shifts in  $\beta/\kappa$ , revealing cases where improved robustness or accuracy does not translate into more human-like generalization geometry. These results demonstrate that RD geometry provides a compact, model-agnostic lens for comparing generalization behavior across systems beyond standard accuracy-based metrics.

---

<sup>1</sup>Windreich Department of AI and Human Health, Icahn School of Medicine at Mount Sinai, New York, NY, USA <sup>2</sup>Department of Computing, Imperial College London, London, UK <sup>3</sup>Department of Psychiatry, Icahn School of Medicine at Mount Sinai, New York, NY, USA <sup>4</sup>Department of Neuroscience, Icahn School of Medicine at Mount Sinai, New York, NY, USA <sup>5</sup>Berkman Klein Center for Internet & Society, Harvard University, Cambridge, MA, USA. Correspondence to: Baihan Lin <baihan.lin@mssm.edu>.

Preprint. March 3, 2026.

## 1. Introduction

Modern vision systems must reliably generalize across transformations of natural images, taking into account texture, contrast, noise statistics, or viewpoint variability that are common in natural visual experience but often underrepresented in training data. Human vision is remarkably robust under such shifts (Geisler, 2008; Burge & Geisler, 2014), whereas standard deep vision models can still fail sharply, exhibiting more brittle behavior under distribution shifts, corruptions, or adversarially structured perturbations (Drenkow et al., 2021; Geirhos et al., 2018; Hendrycks & Dietterich, 2019; Taori et al., 2020; Ilyas et al., 2019). Understanding how these systems generalize and what constraints shape their failures remains a central challenge spanning computer vision, machine learning, and computational neuroscience.

A growing body of work seeks to close these gaps via improved training objectives and data regimes (e.g., invariance-promoting augmentation and pre-training), architectural changes (e.g., transformers), and curriculum-like interventions (Hendrycks et al., 2019; Hernández-García et al., 2019; Shi et al., 2022; Lu et al., 2025). Robustness benchmarks have therefore become a standard tool for assessing out-of-distribution generalization across corruption types and severities (Hendrycks & Dietterich, 2019; Gilmer et al., 2019; Shi et al., 2022). Yet evaluations still summarize behavior primarily through outcome metrics such as accuracy or robustness curves. These measures are indispensable, but limited as diagnostics. They often indicate which system is more robust while obscuring *what trade-off* it makes between fidelity and robustness and *why* failures differ qualitatively. One reason is that accuracy collapses rich error structure into a single number per condition, whereas the *pattern* of confusions can reveal constraints and priorities of the underlying computation.

Cognitive and normative theories offer a principled vocabulary for interpreting this structure. Classical accounts model generalization through similarity geometry in stimulus space (Shepard, 1987; Tenenbaum & Griffiths, 2001; Nosofsky, 1986), while efficient coding and bounded rationality make constraints explicit by casting perception and decision-making as information-limited op-

timization (Attneave, 1954; Barlow et al., 1961; Atick & Redlich, 1992; Simoncelli & Olshausen, 2001; Ortega & Braun, 2013; Todorov, 2004). In this view, confusions and distortions are not merely noise, but signatures of an underlying information–fidelity trade-off, closely related to rational inattention perspectives on systematic errors (Sims, 2018; Jakob & Gershman, 2023a). In machine learning, complementary information-theoretic lenses connect generalization to compression and complexity—from minimum description and code length (Rissanen, 1978; Grünwald, 2007) to PAC-Bayes and information-complexity bounds (McAllester, 1999; Xu & Raginsky, 2017), and representation-learning accounts such as the information bottleneck (Tishby et al., 2000; Alemi et al., 2016). Taken together, these perspectives motivate evaluation tools that directly target the induced trade-off between information and error, not only performance summaries.

Importantly, rate–distortion theory (RDT) (Shannon et al., 1959; Cover & Thomas, 2006) provides a formalism for describing such trade-offs. In classical RDT, an encoder compresses inputs under an information-rate constraint and a decoder reconstructs task-relevant outputs, producing a rate–distortion function  $R(D)$  that relates mutual information to expected distortion under an optimal coding scheme. For our purposes, the key point is not to claim access to an internal code, but to use RDT as a geometric lens for summarizing how a system’s *observable behavior* trades off fidelity and robustness.

Recent work has applied RDT-style analyses to human choice behavior and simple artificial agents, showing that generalization gradients can emerge from constrained channel-like behavior rather than being imposed ad hoc (Sims, 2018; Jakob & Gershman, 2023b). However, it remains unclear whether *humans and modern vision models* exhibit comparable rate–distortion trade-offs on the same natural image tasks, and—crucially for machine learning evaluation—whether such trade-offs reveal structure that is not captured by accuracy-based robustness reporting, especially across architectures, training regimes, and noise conditions.

**Contribution.** We address this gap by introducing a rate–distortion–theoretic *evaluation framework* for visual generalization and applying it to matched human and model behavior on a benchmark dataset with twelve controlled image perturbations. We treat each system—biological or artificial—as an *effective behavioral communication channel* from images to class labels, estimated from empirical confusion matrices. We then use rate–distortion theory to trace each system’s information–error trade-off and summarize its geometry with two interpretable parameters: slope ( $\beta$ ) and curvature ( $\kappa$ ). Together, these form a compact *rate–distortion signature* that characterizes *how* a system’s

errors change as robustness demands increase. This approach yields a model-agnostic diagnostic that complements standard robustness metrics and enables direct comparison between deterministic networks and stochastic human observers by focusing on *behavioral trade-off geometry*.

### 1.1. Rate–distortion theory as a trade-off formalism

Rate–distortion theory (RDT) (Shannon et al., 1959; Cover & Thomas, 2006) provides a formalism for quantifying the minimal information required to achieve a given level of expected error. Let  $X$  denote an input (or stimulus), and let  $\hat{X}$  denote its reconstruction (or an output proxy), with a nonnegative distortion function  $d(x, \hat{x})$ . The resulting rate–distortion function is

$$R(D) = \min_{p(\hat{x}|x): \mathbb{E}[d(X, \hat{X})] \leq D} I(X; \hat{X}), \quad (1)$$

where  $I(X; \hat{X})$  is mutual information and  $D$  is the tolerated expected distortion. Intuitively,  $R(D)$  traces an *optimal frontier*, where achieving lower distortion (higher fidelity) generally requires transmitting more information, and the shape of this frontier captures how rapidly resource demands grow as accuracy requirements tighten.

Motivated by cognitive applications where RDT-style analyses help explain structured confusions and generalization gradients as emergent consequences of constrained information processing (Sims, 2018; Jakob & Gershman, 2023a), we use RDT as an *evaluation lens* applied to observable behavior. We compute behavioral rate–distortion curves by first inferring an experiment-specific cost matrix  $\rho$  from confusions (Sims, 2018), and then numerically tracing  $(D(\lambda), R(\lambda))$  via Blahut fixed-point updates for a grid of  $\lambda$  values (Blahut, 1972; Arimoto, 1972). We summarize the resulting geometry with low-dimensional signatures (slope and curvature) used throughout the evaluation.

Our approach is intentionally *behavioral* and *model-agnostic*. Unlike representation-focused analyses that require access to internal activations or estimation of high-dimensional mutual information, we infer an *effective* trade-off geometry directly from stimulus–response behavior. This enables direct comparison across deterministic networks and stochastic human observers. The resulting “information” quantities we estimate reflect an *effective behavioral channel* rather than a direct measurement of internal representational capacity.

### 1.2. From accuracy–robustness Pareto frontiers to rate–distortion geometry

Robustness research often frames generalization as a Pareto trade-off between clean accuracy and robustness under corruptions or shifts (Hendrycks & Dietterich, 2019; Geirhos et al., 2018; Wichmann & Geirhos, 2023). These empirical

frontiers are useful summaries, but they remain outcome-focused by describing what happens, not how or why a system transitions from stable to brittle behavior as conditions degrade.

RDT provides a trade-off-based analog in which the rate-distortion curve is itself a Pareto frontier between information rate and distortion. Its *slope* quantifies the marginal information cost of reducing distortion, and its *curvature* captures how abruptly a system transitions between coarse and fine-grained behavior. In our formulation, these geometric features become measurable and interpretable signatures that organize humans and models on a shared axis of generalization behavior, complementing accuracy-only robustness reporting.

## 2. Framework: Rate–Distortion Geometry for Behavioral Evaluation

### 2.1. Behavior as an effective channel

For each system  $s$  (human or model), experiment  $e$ , and distortion level  $d$ , we summarize stimulus–response behavior with a  $K \times K$  confusion matrix  $N^{(s,e,d)}$  of counts, where  $N_{ij}$  is the number of trials (or images) with true class  $i$  for which the system responded with class  $j$ . Row-normalizing yields an empirical conditional distribution

$$C_{ij}^{(s,e,d)} = \Pr(y = j \mid x = i; e, d) \approx \frac{N_{ij}^{(s,e,d)}}{\sum_{j'} N_{ij'}^{(s,e,d)}}. \quad (2)$$

We use this row-stochastic matrix  $C^{(s,e,d)}$  as an *effective behavioral channel*  $p_s(y \mid x; e, d)$  for downstream analyses.

For human data,  $N^{(s,e,d)}$  is obtained by aggregating forced-choice trial responses. For models, we compute one predicted label per image (after any required decision mapping to the  $K$ -way label space) and aggregate these *hard decisions* into counts (i.e., our confusion matrices reflect *argmax* predictions rather than probability-averaged responses). Unless otherwise stated, all RD fits and signatures operate on the row-normalized channel  $C^{(s,e,d)}$  derived from these counts.

### 2.2. Behavioral rate–distortion curve estimation

We instantiate Eq. 1 at the behavioral level by treating each system  $s$  as an effective channel from true labels  $x$  to responses  $y$ . For each experiment  $e$  and distortion level  $d$  we obtain an empirical channel  $C^{(s,e,d)} \approx p_s(y \mid x; e, d)$  and trace the corresponding behavioral rate–distortion (RD) curve summarizing the implied information–error trade-off in a manner comparable across humans and models.

**Bayesian inference of the distortion geometry.** Rather than fixing a 0–1 classification loss, we follow the behavioral RD approach of Sims (2018) and treat the distortion (error-cost) structure as a latent quantity inferred from empirical confusions. Specifically, for each experiment we infer a cost matrix  $\rho \in \mathbb{R}_{\geq 0}^{K \times K}$  by maximum a posteriori (MAP) optimization under a structured prior that regularizes symmetric, asymmetric, and diagonal components of  $\rho$ . Given a candidate  $\rho$ , we obtain the corresponding optimal channel  $q_\lambda(y \mid x)$  by Blahut–Arimoto fixed-point updates and evaluate the fit of  $\rho$  by comparing this implied channel to the empirical behavior. This yields an inferred distortion geometry  $\rho(x, y)$  that captures graded structure in the pattern of confusions beyond a binary correct/incorrect loss. Where needed, posterior uncertainty around the MAP estimate can be approximated locally via a Laplace approximation based on the Hessian at the optimum.

**Rate–distortion curve construction.** Given the inferred cost matrix  $\rho$ , we trace a discrete approximation to the rate–distortion frontier by scaling  $\rho$  with an inverse-temperature parameter  $\lambda > 0$  and computing the corresponding optimal channel:

$$q_\lambda(y \mid x) \propto q_\lambda(y) \exp\{-\lambda \rho(x, y)\}. \quad (3)$$

For a log-spaced grid of  $\{\lambda_k\}_k$ , we compute the mutual information  $R_k = I(X; Y)$  and expected distortion  $D_k = \mathbb{E}[\rho(X, Y)]$  under an empirical class prior, yielding rate–distortion points  $\{(D_k, R_k)\}_k$  for each system and experiment. These points provide a curve-level summary of the trade-off geometry implied by the behavioral channel  $C^{(s,e,d)}$  and the inferred distortion structure  $\rho$ .

### 2.3. Rate–distortion signatures

From each estimated rate–distortion frontier  $\{(D_k, R_k)\}_{k=1}^K$ , we extract compact summary statistics that serve as *behavioral signatures* of generalization geometry.

- **Slope ( $\beta$ ).** We estimate local slopes along the frontier by finite differences,  $s_k = (R_{k+1} - R_k)/(D_{k+1} - D_k)$  after sorting by  $D$  and removing duplicate  $D$  values. We summarize slope as  $\beta \equiv \text{median}_k s_k$  (and report the mean as a secondary summary when needed).
- **Curvature proxy ( $\kappa$ ).** We quantify curvature as the dispersion of local slopes,  $\kappa \equiv \text{Var}_k(s_k)$ , which is zero for an exactly linear trade-off and increases as the marginal information cost of reducing distortion varies more strongly across the frontier.
- **AUC.** We compute efficiency as the area under the  $R(D)$  curve over the traced distortion range using trapezoidal integration after filtering non-finite points.

### 3. Evaluation Protocol

#### 3.1. Human vs. Artificial Neural Network Systems

Our primary analysis groups models by *architecture and training paradigm* to probe whether different model classes occupy distinct regions of rate–distortion geometry. This architecture-based organization is designed to support our model-agnostic evaluation question: Do systems with different inductive biases and training paradigms exhibit distinct rate–distortion trade-off geometries, and are these differences consistent across perturbation families?

##### Model architectures.

- **Humans:** human psychophysics observers from the Generalization (GEN, (Geirhos et al., 2018)) and the modelvshuman ModelZoo ((Geirhos et al., 2021)) repositories
- **Supervised CNN baseline models:** standard ImageNet-trained convolutional networks, including GoogLeNet (Szegedy et al., 2015), ResNet-152 (He et al., 2016), and VGG19 (Simonyan & Zisserman, 2014)
- **Large-scale supervised models:** BiT models (bitm-resnetv2-152x2, bitm-resnetv2-152x4 (Kolesnikov et al., 2020))
- **Transformers and vision–language models:** Vision Transformer ViT Large Patch16-224 (Dosovitskiy, 2020), SWAG-ViT-L/16-IN1K (Singh et al., 2022), CLIP (Radford et al., 2021)
- **Architectural inductive-bias probes (LocalModels):** BagNet-9 and BagNet-33 (Brendel & Bethge, 2019)
- **Robustness/shape-biased models:** standard ResNet-50 CNNs trained on Stylized ImageNet (ResNet50 SIN) and a mixture of Stylized and regular ImageNet ResNet50 (SIN+IN) (Geirhos et al., 2018)
- **Data rich semi-supervised models:** semi-weakly supervised pretrained ResNeXt-101 32x16d SWSL (Mahajan et al., 2018), Noisy Student pretraining (efficientnet-l2-noisy-student-475 (Xie et al., 2020))
- **Self-supervised / contrastive models:** Simple Framework for Contrastive Learning models (SimCLR resnet50x1, SimCLR resnet50x4 (Chen et al., 2020a)), MoCo v2 (Chen et al., 2020b), InfoMin (Tian et al., 2020)

##### Training-regimes.

- **Baseline (B).** Standard supervised ImageNet-trained convolutional neural networks (CNNs) evaluated without any robustness-specific intervention: GoogLeNet, ResNet-152, and VGG-19.
- **Distortion-trained (D).** Robustness-trained ResNet-50 variants trained from scratch on a 16-class ImageNet subset with a distorted training distribution. We treat these models as a distinct intervention that changes the training distribution rather than the architecture.
- **Specialised (S).** Single-distortion ResNet-50 models trained from scratch on one perturbation family (e.g., contrast-only or a specific noise type) and then evaluated across all perturbations and severities. This regime targets maximal in-family robustness and typically tests transfer to mismatched perturbations.
- **All-noise / multi-corruption (N).** Multi-distortion ResNet-50 models trained from scratch on mixtures of perturbations (e.g., combining multiple noise-like corruptions, or uniform noise plus another distortion depending on the benchmark variant) and evaluated across individual perturbations. This regime tests whether robustness emerges from exposure to a broader corruption distribution and whether it generalizes beyond the corruption family used in training.

#### 3.2. Benchmark dataset and task

**Stimulus benchmark.** We analyze matched human and model behavior on controlled perturbations of natural images in a 16-way ImageNet-derived categorization setting. The primary stimulus benchmark is the generalization dataset provided by Geirhos and colleagues (Geirhos et al., 2018), which comprises twelve perturbation families (i.e., colour/grayscale, contrast, high-pass, low-pass (blurring), phase noise, power equalisation, opponent colour, rotation, Eidolon I, II and III, and uniform noise). For each perturbation type, images were parameterized by distortion strength, yielding systematic out-of-distribution evaluation conditions (see (Geirhos et al., 2018) for full benchmark details).

**Datasets and experimental setup.** All human and model datasets were obtained from two repositories. The GEN repository (Geirhos et al., 2018) includes human psychophysics data (~83k trials), pretrained supervised CNN baselines, and the set of robustness-training experiments based on ResNet-50 models trained from scratch on a 16-class ImageNet subset under distorted training distributions (including specialised single-distortion and multi-corruption training regimes). The ModelZoo repository (Geirhos et al., 2021) includes a separate human dataset (~85k trials) and a broad set of pretrained architectures spanning architectural inductive-bias probes, large-scale supervised pretraining

families, self-supervised/contrastive CNNs, and transformer and vision–language models.

The GEN human data were collected as a large-scale psychophysics comparison datasets for the original benchmark release, while the ModelZoo human data were designed for consistent model–human comparability with matched stimulus presentations. All humans and models were evaluated on the same 16-way categorization task across experimental perturbation and distortions. Response distributions and confusion matrices were estimated for each experiment from forced-choice responses of empirical trial counts (humans), predicted labels (GEN repository models), or the evaluation of pretrained checkpoints using the `modelvshuman` toolbox (Geirhos et al., 2021) (all ModelZOO models).

## 4. Results

We report results in four steps. First, we validate that RDT provides a faithful behavioral account of confusion structure and generalization gradients across systems. Second, we characterize how architecture families occupy distinct regions of rate–distortion geometry. Third, we test how training interventions shift systems in RD space. Finally, we summarize the global organization of signatures across perturbations and systems. Detailed statistical analyses are reported in the Appendix A.1.

### 4.1. Model validity: Do humans and deep vision models behaviorally conform to rate-distortion theory?

**Generalization curves.** We first test whether both human and model behavior are well described by an effective behavioral rate–distortion (RDT) channel, and whether architectures and training regimes exhibit systematic departures from the simplest exponential generalization law. Across systems, RDT successfully captures the dominant structure of confusions and generalization gradients with consistently low error  $\text{RMSE} = 0.078$ ; see Appendix B for all values). Figure 1a shows empirical generalization probabilities  $G(x, \hat{x})$  as a function of inferred error cost  $\rho$ , together with the corresponding RDT-predicted curves. Qualitatively, humans show a gradual decay in generalization with increasing cost, while model families vary in the sharpness of this drop-off.

**Rate–distortion fit diagnostics.** We quantify goodness-of-fit with two complementary RMSE diagnostics (Appendix B). (i) *Channel-fit (confusion) diagnostic*: RMSE between observed and RDT-predicted *off-diagonal* confusion probabilities. This pooled error is small across families (range  $\approx 0.010$  to  $0.032$ ). For example, it is lowest for All-noise (0.010) and Specialised (0.011), modest for Baseline CNNs (0.014) and Humans (0.018), and highest among the families shown for Local Models (0.032). This indicates

that an effective RDT channel explains most of the observed confusion structure, while residuals remain structured and family-dependent.

(ii) *Gradient-shape diagnostic*: RMSE between the empirical binned generalization gradient  $G_{\text{emp}}(d)$  and its best-fit exponential approximation  $ae^{-sd}$ . These errors are likewise small overall (range  $\approx 0.004$  to  $0.047$ ) but show clearer separation between families: Humans (0.008) and All-noise (0.004) are close to exponential, Baseline CNNs are higher (0.031), and the largest deviations among the shown families occur for Vision Transformers (0.047) and Local Models (0.043). Thus, while confusion structure is broadly well captured across systems, the *shape* of the generalization gradient exhibits systematic, architecture- and training-dependent departures from a single exponential law.

### 4.2. Model families occupy distinct regions of rate–distortion geometry relative to humans

We asked whether architectures form distinct *rate–distortion (RD) signatures* relative to humans by comparing model families to human behavior *within matched perturbation contexts* (blocks;  $n_{\text{blocks}} = 73$ ). Across blocks, non-human families consistently occupy shifted regions of RD space, with reliably steeper slopes and (in most cases) higher curvature than humans (Fig. 2a; statistics in Table 2). In particular, LOCALMODELS and SHAPEBIASED showed the largest slope offsets and curvature differences, whereas VISIONTRANSFORMERS were closest to humans in curvature.

Differences in curvature were even more pronounced. LOCALMODELS showed substantially higher  $\kappa$  than humans ( $\Delta\kappa = 1.46$ ,  $\approx 28.8\times$ ,  $p_{\text{FDR}} < 10^{-11}$ ), and SHAPEBIASED, SELFSUPERVISED, SEMISUPERVISED, and LARGE CNNs also exhibited higher  $\kappa$  than humans (median  $\Delta\kappa \in [0.115, 0.340]$ , folds  $\approx 1.30\times$  to  $\approx 2.19\times$ ; all  $p_{\text{FDR}} < 0.02$ ). In contrast, VISIONTRANSFORMERS were not distinguishable from humans in  $\kappa$  ( $\Delta\kappa = -0.014$ ,  $p_{\text{FDR}} = 0.18$ ). These family-level patterns are consistent with model-level paired comparisons reported in Appendix Table 2.

### RD parameters provide information beyond accuracy.

To test whether RD geometry captures structure beyond conventional performance, we investigated whether family offsets in  $\beta$  and  $\kappa$  persist after accounting for accuracy. This showed that RD geometry partially dissociates from conventional performance. Some models match humans in accuracy yet differ strongly in RD parameters (e.g., CLIP: ( $\Delta\text{Acc} = 0.0246$ ,  $p_{\text{FDR}} = 0.11$ ;  $\Delta\beta = 0.140$ ,  $p_{\text{FDR}} < 10^{-3}$ ;  $\Delta\kappa = 0.280$ ,  $p_{\text{FDR}} < 10^{-4}$ ), consistent with the separation visible in Fig. 2a. To test whether these geometry shifts persist beyond accuracy, we fit block fixed-effects regressions predicting  $\beta$  and  $\kappa$  from within-block accuracy and architecture-family indicators (humans as ref-

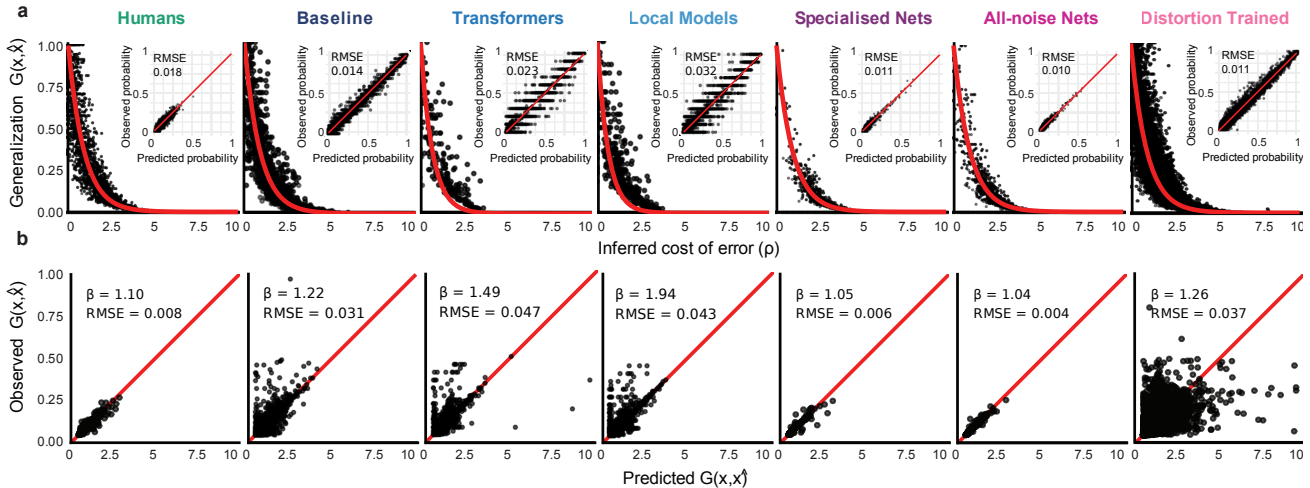


**Figure 1. Generalization curves and goodness-of-fit of rate–distortion predictions.** (a) Empirical generalization  $G(x, \hat{x})$  (points) plotted against inferred cost of error  $\rho$  for humans and selected model families. Red curves show the corresponding exponential/RD-style prediction. Insets show observed vs. predicted off-diagonal confusion probabilities (RDT channel prediction), with RMSE reported per family. (b) Summary of exponential-gradient fits: observed binned generalization gradients versus predictions from the best-fit  $a e^{-s d}$  model (red diagonal indicates equality). Each panel reports the fitted slope  $s$  and RMSE, quantifying family-specific deviations from a simple exponential generalization law.

erence; Table 2). Even though accuracy is negatively associated with both RD parameters, but architecture-family offsets remain reliably positive, demonstrating that RD geometry captures systematic, family-structured variation not explained by accuracy alone. Moreover, interaction tests provide little evidence that families differ in the *form* of the accuracy–geometry relationship, suggesting that architectures primarily differ by their *location* in RD space rather than by changes in how accuracy maps onto RD geometry.

### 4.3. Robustness training moves models in RD space along different axes of “human-likeness”

We next tested whether robustness-oriented training interventions systematically shift models’ locations in RD space toward (or away from) humans. For this we focus on the GEN regimes that enable controlled training comparisons and evaluate each regime against humans within matched experiment–condition blocks (Fig. 2; statistics in Table 3).

**Baseline CNNs remain geometrically separated from humans.** Across matched blocks, classically pretrained CNNs (GoogLeNet, ResNet-152, VGG-19) occupy a distinct RD regime relative to humans. All three models show reliably larger  $\beta$  and  $\kappa$  (Table 3) and reduced RD efficiency (AUC;  $\Delta\text{AUC} \approx -0.02$ ,  $q \leq 10^{-5}$ ). This systematic displacement from the human cluster is evident in Fig. 2, indicating sharper, more curved trade-offs even when accuracy differences are small.

**Distortion-trained models move toward humans in geometry but lose performance.** The distortion-trained regime partially closes the geometric gap, with smaller (though still significant) offsets in  $\beta$  and  $\kappa$  relative to humans (e.g.,  $\Delta\beta = 0.188$ ,  $q = 1.31 \times 10^{-5}$ ; Table 3), consistent with a shift toward the human region in Fig. 2. However, this geometric movement comes at a cost: both accuracy and AUC decrease relative to humans ( $q < 10^{-2}$  and  $q < 10^{-4}$ , respectively; Table 3).

**All-noise and specialised training improve accuracy/efficiency, but overshoot along curvature.** Multi-corruption (*all-noise*) and single-corruption (*specialised*) regimes show the opposite dissociation. Both outperform humans in accuracy ( $q < 10^{-5}$ ) and modestly increase AUC (Table 3). Yet their slope shifts are small and not distinguishable from humans after correction, while curvature shifts past humans in the opposite direction (both  $\Delta\kappa < 0$ ,  $q < 10^{-3}$ ). This shows that robustness interventions can improve performance and efficiency while moving models toward humans along the slope axis but away from humans along the curvature axis. This is a trade-off visible in Fig. 2 as well and not recoverable from accuracy alone.

To illustrate how RD geometry changes *within* an experiment as perturbation severity increases, Appendix A.2 analyzes the noise-severity conditions and plots each system’s inferred  $\beta$  as a function of noise level (Fig. 3), revealing that systems can share the same direction of  $\beta$  change with severity while differing markedly in the *dynamics* (gradual vs. abrupt transitions).

**Do interventions change the accuracy–geometry relationship, or mainly shift location in RD space?** Finally, we asked whether training regimes *change the coupling* between performance and RD geometry, or instead *translate* systems within a shared landscape. After controlling for matched blocks, accuracy is negatively associated with both RD slope and curvature, while regime-specific offsets persist (Table 3). Crucially, we find no evidence that regimes alter the *form* of the accuracy–geometry relationship (interaction tests: both  $p > 0.4$ ), implying that interventions primarily shift a model’s *location* in RD space rather than changing how accuracy maps onto geometry. This “translation” view is visually supported by Fig. 2b, where each family/regime forms a coherent band in  $(\beta_n, \kappa_n)$  with similar orientation, but displaced intercepts.

#### 4.4. Global approximation of the Pareto frontier

The paired tests above establish reliable *within-block* separations between humans and model families. We next ask a global question: across systems and perturbation contexts, do RD signatures organize behavior along an approximate Pareto surface linking fidelity, efficiency, and trade-off shape? Fig. 2b provides a compact visualization of this structure by plotting standardized slope vs. curvature ( $\beta_n$  vs.  $\kappa_n$ ) and encoding efficiency (AUC) by color.

#### Families occupy coherent regions of the frontier.

Across perturbations, families cluster into distinct regions of  $(\beta_n, \kappa_n, \text{AUC})$  space. Humans concentrate in a low-slope, low-curvature region, while baseline CNNs and many ModelZoo families occupy systematically steeper and/or more curved regions. This separation is visible as family-specific clouds and bands in Fig. 2b.

#### The geometry is structured but not one-dimensional.

Although slope and curvature often covary, Fig. 2b shows that they are not interchangeable. Regimes can approach humans along one axis while diverging along the other. Concretely, the robustness regimes illustrate axis-specific “human-likeness”. All-noise and specialised training sit near humans along the slope axis (similar  $\beta_n$ ), yet shift away along curvature, whereas distortion-trained models shift toward humans in geometry more broadly but at lower efficiency (cooler AUC colors).

#### Efficiency gains need not imply human-like geometry.

Finally, the global view highlights that improvements in efficiency (higher AUC) can coincide with non-human shifts in trade-off *shape*. In Fig. 2b, regimes with higher AUC are not consistently closest to the human region in  $(\beta_n, \kappa_n)$ , reinforcing the central point: robustness interventions can improve performance and efficiency while moving systems along different geometric directions on the frontier.

## 5. Discussion

Prior cognitive-science work has established deep links between efficient coding, generalization gradients, and RD structure in human behavior (Sims, 2018). The main contribution of this paper is the *scaling and operationalization* of these ideas into a model-agnostic evaluation tool for modern vision systems, and in showing that—like humans—a wide range of deep vision networks exhibit consistent rate–distortion trade-offs during perceptual generalization. This is enabled by (i) a unified behavioral-channel construction that applies to humans and heterogeneous architectures without inspecting internal activations, and (ii) compact RD signatures that expose stable family-level separations and regime-induced translations across many perturbation contexts. Crucially, the training-regime results show that “human-likeness” is *axis-dependent*: distortion-training shifts geometry toward humans while reducing accuracy/efficiency, whereas all-noise and specialised training can improve accuracy/efficiency while shifting curvature past humans. This dissociation motivates treating  $(\beta, \kappa, \text{AUC})$  as complementary diagnostics that reveal intervention-sensitive structure not recoverable from accuracy-only robustness summaries.

#### Pareto-frontier view: RD signatures as local coordinates on a trade-off surface.

Rate–distortion theory formalizes an optimal frontier between expected distortion and information rate (Shannon et al., 1959; Cover & Thomas, 2006). In our behavioral instantiation, each system induces an *effective* trade-off surface whose geometry can be summarized by local coordinates. Median slope  $\beta$  captures the typical marginal “rate cost” of reducing distortion in the traced regime, while curvature proxy  $\kappa$  captures how *non-uniform* that marginal cost is across the frontier. This sharpens a common robustness intuition. Namely, that two systems can match in average performance or efficiency yet differ in whether gains accrue smoothly (smaller  $\kappa$ ) or via brittle transitions (larger  $\kappa$ ). Together with AUC as an efficiency summary over the traced range, these coordinates provide a compact way to compare where systems sit on the trade-off surface and how training interventions translate them along different directions.

#### Generalization efficiency as an actionable diagnostic.

From an evaluation standpoint, “generalization efficiency” is not a single number. Instead, it decomposes into (i) *where* a system sits on the trade-off surface (AUC / overall efficiency), and (ii) *how* it moves along that surface as conditions worsen (slope and curvature). This decomposition suggests concrete uses for practitioners. First, RD signatures enable *model selection under constraints*. When two models achieve similar accuracy, prefer the one with lower  $\kappa$  if smooth degradation across conditions is desirable (e.g.,

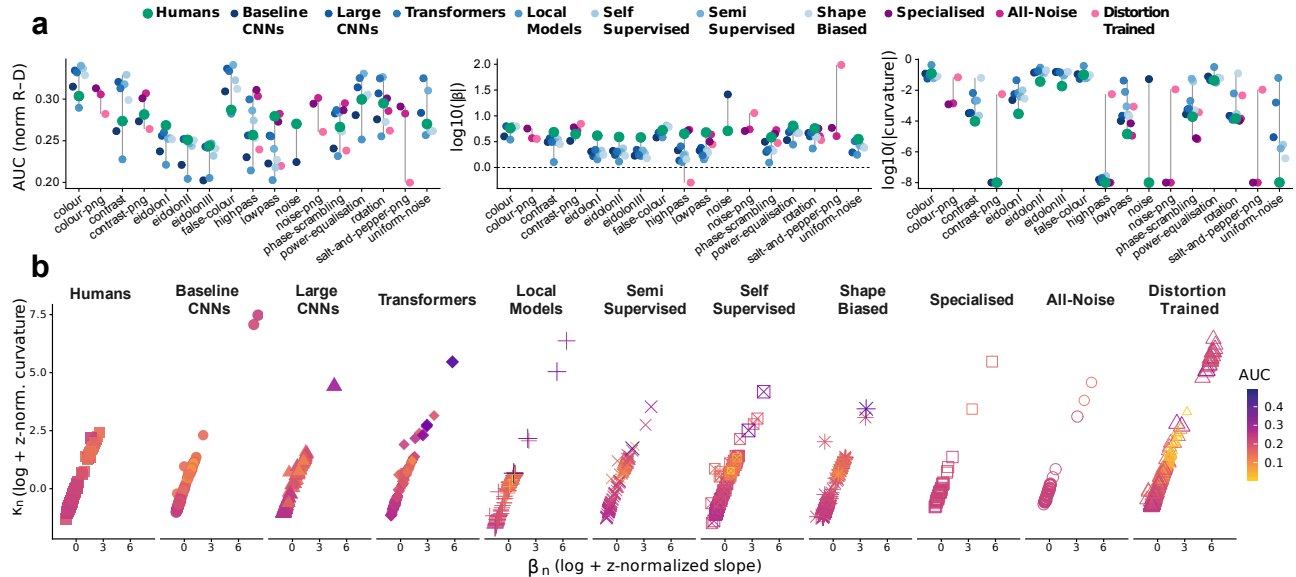


**Figure 2. Rate–distortion signatures across perturbation experiments and system families.** (a) For each experiment/condition (x-axis; abbreviations as shown), points show systems’ RD summaries: normalized rate–distortion efficiency (AUC; left),  $\log_{10} |\beta|$  (middle), and  $\log_{10} |\kappa|$  (right), grouped by family/regime (legend). Values are computed per experiment  $\times$  condition block and visualized to highlight between-family structure across contexts. (b) Global view of the behavioral trade-off landscape: block-level  $\beta_n$  (log- and z-normalized slope) vs.  $\kappa_n$  (log- and z-normalized curvature), faceted by family/training-regime. Marker color encodes AUC. Across families, points form coherent bands with similar orientation but different intercepts, consistent with a shared accuracy–geometry coupling and family/regime-dependent *location shifts* in RD space.

safety-critical perception), or prefer higher AUC if overall efficiency in the evaluated regime is the goal. Second, RD signatures provide a principled way to quantify *training side effects*. Robustness interventions may improve accuracy and AUC while moving curvature past humans in the opposite direction, indicating a different and less human-like “character” of generalization even when performance improves.

**Extension to adversarially trained and robustness-trained networks.** A natural next step is to apply the same pipeline to adversarially trained and certified-robust models. Conceptually, adversarial training can be viewed as altering the effective distortion geometry by emphasizing worst-case or high-cost confusions. RD signatures would then quantify whether such training induces (i) increased efficiency for adversarial neighborhoods (AUC gains), (ii) a shift in typical marginal cost (changes in  $\beta$ ), and crucially, (iii) whether robustness comes from smoother trade-offs (reduced  $\kappa$ ) or from sharper regime boundaries (increased  $\kappa$ ). RD signatures can distinguish robustness strategies that yield similar adversarial accuracy but qualitatively different degradation profiles under perturbation strength, transfer, or combined shifts.

**Limitations and future work.** It is important to emphasize that our “rate” is explicitly behavioral.  $I(X; Y)$  is

computed from output confusion statistics and should be interpreted as an effective stimulus–response rate under a specified task and cost geometry, not as mutual information in internal representations. This makes modeling choices—including Laplace smoothing strength  $a$ , cost inference vs. fixed distortion (e.g., 0–1), the assumed class prior, and the traced  $\lambda$  grid—important targets for sensitivity analyses that should be explored in future work to further assess the robustness and portability of the RD signatures. Moreover, the present study focuses on a single controlled perturbation suite and a 16-way task, leaving open how stable ( $\beta$ ,  $\kappa$ , AUC) remain under changes in dataset semantics, label granularity, or long-tailed priors. Promising next steps are therefore to (i) test stability across additional benchmarks, natural distribution shifts, and alternative label resolutions, (ii) extend coverage to modern robustness paradigms, including adversarially trained and certified models, and (iii) where possible, relate behavioral RD geometry to internal representational structure to clarify when effective-channel differences track mechanistic differences in learned representations.

## 6. Conclusion

We present a behavioral RD evaluation framework that converts confusion statistics into an effective RD frontier via an effective channel and summarize its trade-off geometry

with compact signatures of generalization geometry. Across humans and diverse modern deep vision models of varying architectures and training regimes, these signatures (slope  $\beta$ , curvature proxy  $\kappa$ , and AUC) provide a unified language for comparing *how* systems trade performance for robustness, revealing stable model family-level separations and training-induced shifts that are not explained by accuracy alone.

## Acknowledgments

This work was supported in part through the Minerva computational and data resources and staff expertise provided by Scientific Computing and Data at the Icahn School of Medicine at Mount Sinai and supported by the Clinical and Translational Science Awards (CTSA) grant UL1TR004419 from the National Center for Advancing Translational Sciences. BL is supported by the U.S. National Institutes of Health (NIH), the U.S. Department of Veterans Affairs (VA), the Brain & Behavior Research Foundation (BBRF), The Sidney R. Baer, Jr. Foundation, the Hasso Plattner Foundation, and the Windreich Family Foundation. No funding was specific to this work.

## Impact Statement

This paper presents work whose goal is to advance the field of Machine Learning. There are many potential societal consequences of our work, none which we feel must be specifically highlighted here.

## References

- Alemi, A. A., Fischer, I., Dillon, J. V., and Murphy, K. Deep variational information bottleneck. *arXiv preprint arXiv:1612.00410*, 2016.
- Arimoto, S. An algorithm for computing the capacity of arbitrary discrete memoryless channels. *IEEE Transactions on Information Theory*, 18(1):14–20, 1972.
- Atick, J. J. and Redlich, A. N. What does the retina know about natural scenes? *Neural computation*, 4(2):196–210, 1992.
- Attneave, F. Some informational aspects of visual perception. *Psychological review*, 61(3):183, 1954.
- Barlow, H. B. et al. Possible principles underlying the transformation of sensory messages. *Sensory communication*, 1(01):217–233, 1961.
- Blahut, R. Computation of channel capacity and rate-distortion functions. *IEEE Transactions on Information Theory*, 18(4):460–473, 1972. doi: 10.1109/TIT.1972.1054855.
- Brendel, W. and Bethge, M. Approximating cnns with bag-of-local-features models works surprisingly well on imagenet. *arXiv preprint arXiv:1904.00760*, 2019.
- Burge, J. and Geisler, W. S. Optimal disparity estimation in natural stereo images. *Journal of vision*, 14(2):1–1, 2014.
- Chen, T., Kornblith, S., Norouzi, M., and Hinton, G. A simple framework for contrastive learning of visual representations. In *International conference on machine learning*, pp. 1597–1607. PmLR, 2020a.
- Chen, X., Fan, H., Girshick, R., and He, K. Improved baselines with momentum contrastive learning. *arXiv preprint arXiv:2003.04297*, 2020b.
- Cover, T. M. and Thomas, J. A. *Elements of Information Theory*. Wiley, 2nd edition, 2006.
- Dosovitskiy, A. An image is worth 16x16 words: Transformers for image recognition at scale. *arXiv preprint arXiv:2010.11929*, 2020.
- Drenkow, N., Sani, N., Shpitser, I., and Unberath, M. A systematic review of robustness in deep learning for computer vision: Mind the gap? *arXiv preprint arXiv:2112.00639*, 2021.
- Geirhos, R., Rubisch, P., Michaelis, C., Bethge, M., Wichmann, F. A., and Brendel, W. Imagenet-trained cnns are biased towards texture; increasing shape bias improves accuracy and robustness. In *International conference on learning representations*, 2018.
- Geirhos, R., Narayanappa, K., Mitzkus, B., Thieringer, T., Bethge, M., Wichmann, F. A., and Brendel, W. Partial success in closing the gap between human and machine vision. *Advances in Neural Information Processing Systems*, 34:23885–23899, 2021.
- Geisler, W. S. Visual perception and the statistical properties of natural scenes. *Annu. Rev. Psychol.*, 59(1):167–192, 2008.
- Gilmer, J., Ford, N., Carlini, N., and Cubuk, E. Adversarial examples are a natural consequence of test error in noise. In *International Conference on Machine Learning*, pp. 2280–2289. PMLR, 2019.
- Grünwald, P. D. *The minimum description length principle*. MIT press, 2007.
- He, K., Zhang, X., Ren, S., and Sun, J. Deep residual learning for image recognition. In *Proceedings of the IEEE conference on computer vision and pattern recognition*, pp. 770–778, 2016.

- Hendrycks, D. and Dietterich, T. Benchmarking neural network robustness to common corruptions and perturbations. *arXiv preprint arXiv:1903.12261*, 2019.
- Hendrycks, D., Lee, K., and Mazeika, M. Using pre-training can improve model robustness and uncertainty. In *International conference on machine learning*, pp. 2712–2721. PMLR, 2019.
- Hernández-García, A., König, P., and Kietzmann, T. C. Learning robust visual representations using data augmentation invariance. *arXiv preprint arXiv:1906.04547*, 2019.
- Ilyas, A., Santurkar, S., Tsipras, D., Engstrom, L., Tran, B., and Madry, A. Adversarial examples are not bugs, they are features. *Advances in neural information processing systems*, 32, 2019.
- Jakob, A. M. and Gershman, S. J. Rate-distortion theory of neural coding and its implications for working memory. *Elife*, 12:e79450, 2023a.
- Jakob, A. M. and Gershman, S. J. Rate-distortion theory of neural coding and its implications for working memory. *Elife*, 12:e79450, 2023b.
- Kolesnikov, A., Beyer, L., Zhai, X., Puigcerver, J., Yung, J., Gelly, S., and Houlsby, N. Big transfer (bit): General visual representation learning. In *European conference on computer vision*, pp. 491–507. Springer, 2020.
- Lu, Z., Thorat, S., Cichy, R. M., and Kietzmann, T. C. Adopting a human developmental visual diet yields robust, shape-based ai vision. *arXiv preprint arXiv:2507.03168*, 2025.
- Mahajan, D., Girshick, R., Ramanathan, V., He, K., Paluri, M., Li, Y., Bharambe, A., and Van Der Maaten, L. Exploring the limits of weakly supervised pretraining. In *Proceedings of the European conference on computer vision (ECCV)*, pp. 181–196, 2018.
- McAllester, D. A. Pac-bayesian model averaging. In *Proceedings of the twelfth annual conference on Computational learning theory*, pp. 164–170, 1999.
- Nosofsky, R. M. Attention, similarity, and the identification–categorization relationship. *Journal of experimental psychology: General*, 115(1):39, 1986.
- Ortega, P. A. and Braun, D. A. Thermodynamics as a theory of decision-making with information-processing costs. *Proceedings of the Royal Society A: Mathematical, Physical and Engineering Sciences*, 469(2153):20120683, 2013.
- Radford, A., Kim, J. W., Hallacy, C., Ramesh, A., Goh, G., Agarwal, S., Sastry, G., Askell, A., Mishkin, P., Clark, J., et al. Learning transferable visual models from natural language supervision. In *International conference on machine learning*, pp. 8748–8763. PMLR, 2021.
- Rissanen, J. Modeling by shortest data description. *Automatica*, 14(5):465–471, 1978.
- Shannon, C. E. et al. Coding theorems for a discrete source with a fidelity criterion. *IRE Nat. Conv. Rec.*, 4(142-163): 1, 1959.
- Shepard, R. N. Toward a universal law of generalization for psychological science. *Science*, 237(4820):1317–1323, 1987.
- Shi, Y., Daunhawer, I., Vogt, J. E., Torr, P., and Sanyal, A. How robust are pre-trained models to distribution shift? In *ICML 2022: Workshop on Spurious Correlations, Invariance and Stability*, 2022.
- Simoncelli, E. P. and Olshausen, B. A. Natural image statistics and neural representation. *Annual review of neuroscience*, 24(1):1193–1216, 2001.
- Simonyan, K. and Zisserman, A. Very deep convolutional networks for large-scale image recognition. *arXiv preprint arXiv:1409.1556*, 2014.
- Sims, C. R. Efficient coding explains the universal law of generalization in human perception. *Science*, 360(6389): 652–656, 2018.
- Singh, M., Gustafson, L., Adcock, A., de Freitas Reis, V., Gedik, B., Kosaraju, R. P., Mahajan, D., Girshick, R., Dollár, P., and Van Der Maaten, L. Revisiting weakly supervised pre-training of visual perception models. In *Proceedings of the IEEE/CVF Conference on Computer Vision and Pattern Recognition*, pp. 804–814, 2022.
- Szegedy, C., Liu, W., Jia, Y., Sermanet, P., Reed, S., Anguelov, D., Erhan, D., Vanhoucke, V., and Rabinovich, A. Going deeper with convolutions. In *Proceedings of the IEEE conference on computer vision and pattern recognition*, pp. 1–9, 2015.
- Taori, R., Dave, A., Shankar, V., Carlini, N., Recht, B., and Schmidt, L. Measuring robustness to natural distribution shifts in image classification. *Advances in Neural Information Processing Systems*, 33:18583–18599, 2020.
- Tenenbaum, J. B. and Griffiths, T. L. Generalization, similarity, and bayesian inference. *Behavioral and brain sciences*, 24(4):629–640, 2001.
- Tian, Y., Sun, C., Poole, B., Krishnan, D., Schmid, C., and Isola, P. What makes for good views for contrastive

learning? *Advances in neural information processing systems*, 33:6827–6839, 2020.

Tishby, N., Pereira, F. C., and Bialek, W. The information bottleneck method. *arXiv preprint physics/0004057*, 2000.

Todorov, E. Optimality principles in sensorimotor control. *Nature neuroscience*, 7(9):907–915, 2004.

Wichmann, F. A. and Geirhos, R. Are deep neural networks adequate behavioral models of human visual perception? *Annual review of vision science*, 9(1):501–524, 2023.

Xie, Q., Luong, M.-T., Hovy, E., and Le, Q. V. Self-training with noisy student improves imagenet classification. In *Proceedings of the IEEE/CVF conference on computer vision and pattern recognition*, pp. 10687–10698, 2020.

Xu, A. and Raginsky, M. Information-theoretic analysis of generalization capability of learning algorithms. *Advances in neural information processing systems*, 30, 2017.

## A. Appendix.

### A.1. Statistical analysis

We analyze rate–distortion summary metrics—slope  $\beta$ , curvature  $\kappa$ , area under the RD curve (AUC), and accuracy—as outcomes computed for each system (human or model) within each experimental context. An experimental context (a *block*) is defined as a matched `experiment`  $\times$  `condition` pair. Within each block, different systems evaluated on the same stimuli constitute repeated measurements, enabling paired (block-aware) inference via within-block contrasts. Where applicable, we use the within-experiment normalization defined in Sec. 2.3, control false discoveries using Benjamini–Hochberg (BH–FDR), and report median blockwise differences and rank-biserial correlations as effect-size summaries. Full test tables (including  $n_{\text{blocks}}$  and adjusted  $p$ -values) are provided in the Appendix.

**ModelZoo repository: fully crossed block set.** In the ModelZoo datasets, all humans and models have data for matched stimuli across experiments, so comparisons can be performed on an identical block set throughout.

**GEN repository: unbalanced block set.** In the GEN repository, training-regime datasets are not fully crossed. Therefore, each regime comparison is restricted to the subset of *matched* blocks for the two systems being contrasted. Throughout, we define  $\Delta$  as (regime – humans) and perform inference across the shared blocks. Because unlike other regimes, the distortion-trained regime contains multiple trained instances per block (e.g., 20 models), we first collapse these values within each block (median across instances) before computing regime-level contrasts. We then perform statistical testing at three levels.

1. **Model-by-model comparisons to humans.** For each model, we computed within-block differences to humans,  $\Delta m_b = m_{b,\text{model}} - m_{b,\text{human}}$ , and tested whether the median difference is nonzero using a paired Wilcoxon signed-rank test across blocks.
2. **Family-level pairwise tests.** To test higher-level separations across model families or regimes, we aggregated within each block  $\times$  family/regime to a single median value and performed paired Wilcoxon signed-rank tests for the planned contrasts.

**Accuracy-adjusted fixed-effects regressions and nested interaction tests.** To test whether RD geometry differs across families beyond what is explained by accuracy, we fit within-block fixed-effects regressions using block-demeaned variables,  $\beta_r \sim \text{acc}_r + \text{family}_r + \text{block}$ , where  $\text{acc}_r$  and  $\beta_r$  (and, analogously,  $\kappa_r$ ) are residualized by subtracting within-block means. We then test whether the coupling between accuracy and RD geometry differs by family via nested-model interaction tests, comparing the regression model to the corresponding additive model using ANOVA for nested OLS models. These tests distinguish shifts in *location* in RD space (family offsets) from changes in the *accuracy–geometry relationship* (interaction effects).

### A.2. RD slope responses across severity

Certain perturbations—including phase scrambling, severe noise, and extreme contrast reductions—systematically increase compression demands for all systems. Across experiments, increasing perturbation strength steepens the inferred RD slope signature  $\beta$  (paired tests across experiments,  $p \approx 0.02$ ), indicating that higher information rates are required to maintain accuracy as inputs become less reliable. While this monotonic “difficulty– $\beta$ ” trend has been documented in human generalization (Sims, 2018), our results show that many artificial vision models exhibit the same *direction* of change. However, matching the direction of the effect does not imply matching its *dynamics*, since different systems can reach high-compression regimes either gradually or abruptly as conditions worsen.

To make these dynamics explicit, we analyze a perturbation setting where severity is explicitly parametrized by a continuous corruption scale. Specifically, we focus on a uniform-noise experiment in which increasing noise level acts as a within-experiment stress test on the effective channel. For each system and each noise level, we compute a slope  $\beta$  by regressing the log-probability of off-diagonal confusions against the inferred cost of error  $\rho$ , pooling all off-diagonal class pairs within the corresponding fit. Because some off-diagonal entries can be zero at particular noise levels, we apply additive pseudocount (Laplace) smoothing only for this visualization step, and then row-normalize to obtain probabilities:

$$\tilde{C}_{ij} = \frac{N_{ij} + \alpha}{\sum_{j'} (N_{ij'} + \alpha)}, \quad (4)$$

where  $N_{ij}$  denotes the raw confusion *count* for true class  $i$  and response  $j$ , and we use a fixed pseudocount  $\alpha = 0.5$ . This smoothing is used only to stabilize log-probabilities in the severity plots and is not used in RD fitting or in the primary RD signatures.

Figure 3 shows that humans exhibit a gradual steepening of  $\beta$  with increasing noise. This means that as the visual input becomes less reliable, the effective channel increases the marginal information cost of accuracy in a relatively smooth manner. By contrast, baseline CNNs show a markedly sharper increase in  $|\beta|$  across the same corruption range, consistent with a more abrupt transition into a high-compression regime. Notably, specialised and all-noise networks can exhibit especially steep slopes at intermediate-to-high noise levels, indicating that even when models match the *direction* of the severity effect, they can diverge substantially from humans in how sensitively (and how abruptly) their generalization geometry changes across the corruption scale.

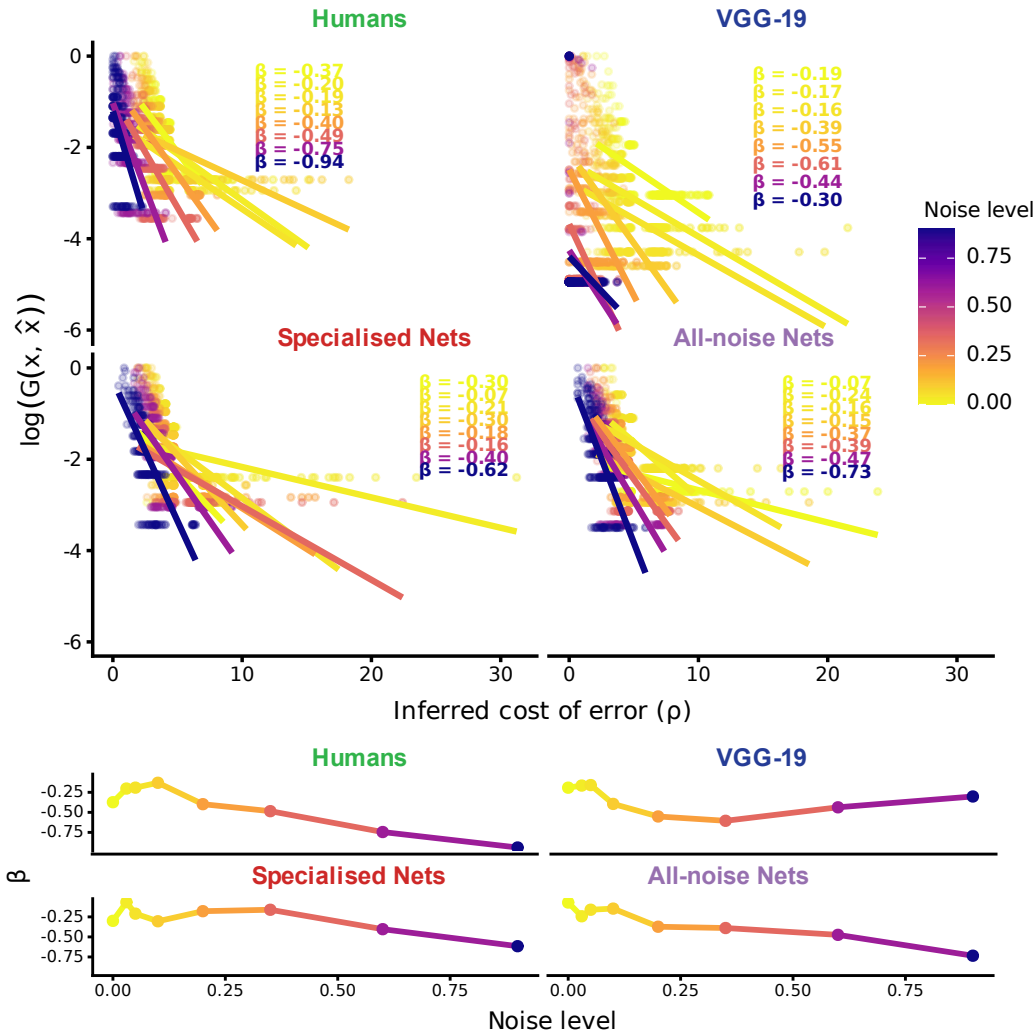


Figure 3. **Effects of noise on generalization slopes across humans and models.** Top panels show, for each system, the relationship between inferred error cost ( $\rho$ ) and the log-probability of off-diagonal confusions, with colored lines denoting different uniform-noise levels. Each line’s slope defines  $\beta$  for that noise level. Confusion counts are stabilized with an additive pseudocount ( $\alpha = 0.5$ ) before row-normalization for this visualization. Bottom panels plot  $\beta$  as a function of noise level, revealing gradual severity dependence in humans and sharper, more noise-sensitive transitions in baseline CNNs, with specialised and all-noise networks exhibiting intermediate patterns.

## B. RMSE Goodness-of-Fit Summary

*Table 1. RMSE-based goodness-of-fit by model family.* For each model family we report the number of fitted files and three complementary RMSE measures: (i) deviation from the rate-matched exponential generalization curve  $G = \exp(-s\rho)$  (RMSE\_GenExp\_median), (ii) observed vs. predicted off-diagonal confusion probabilities (RMSE\_ConfProb), and ... (iii) deviation between the empirical binned generalization gradient and its best-fit exponential form  $a e^{-s^d}$  (RMSE\_Emp\_mean). Lower RMSE indicates better agreement with the corresponding rate-distortion prediction.

Model Family	#files	RMSE_GenExp_median	RMSE_ConfProb	RMSE_Emp_mean
All-noise	53	0.007	0.010	0.004
Baseline	243	0.049	0.014	0.031
Fine-tuned	1220	0.052	0.011	0.029
Humans	154	0.023	0.018	0.008
LargeCNNs	146	0.030	0.027	0.029
LocalModels	146	0.491	0.032	0.043
SelfSupervised	292	0.048	0.025	0.038
SemiSupervised	146	0.034	0.024	0.041
ShapeBiased	146	0.090	0.031	0.025
Specialised	53	0.009	0.011	0.006
VisionTransformers	219	0.025	0.023	0.047

Table 2. **Model-level paired comparisons vs humans and fixed-effects tests of RD geometry beyond accuracy.** Panel A reports paired, within-block differences (model – humans) across  $n_{\text{blocks}} = 73$  matched contexts using two-sided Wilcoxon signed-rank tests.  $q$  denotes BH–FDR-adjusted  $p$ -values (adjusted within each metric across the 15 model contrasts). Panel B reports fixed-effects regressions of RD parameters on within-block accuracy and architecture-family indicators with block fixed effects (block coefficients omitted).

**Panel A: Model-by-model paired comparisons vs humans (Wilcoxon signed-rank;  $n_{\text{blocks}} = 73$ ).**

Model	$\Delta\text{Acc}$	$q_{\text{Acc}}$	$\Delta\beta$ (fold)	$q_{\beta}$	$\Delta\kappa$ (fold)	$q_{\kappa}$	$\Delta\text{AUC}$	$q_{\text{AUC}}$
BagNet-9	-0.339	$< 10^{-4}$	+0.432 ( $\times 2.71$ )	$< 10^{-4}$	+1.900 ( $\times 79.43$ )	$< 10^{-4}$	-0.0554	$< 10^{-4}$
BagNet-33	-0.104	$< 10^{-4}$	+0.308 ( $\times 2.03$ )	$< 10^{-4}$	+0.911 ( $\times 8.15$ )	$< 10^{-4}$	-0.0283	$< 10^{-4}$
ViT-L/16	+0.104	$< 10^{-4}$	+0.062 ( $\times 1.15$ )	0.13	-0.095 ( $\times 0.80$ )	0.42	+0.0355	$< 10^{-4}$
EffNet-L2	+0.115	$< 10^{-4}$	+0.068 ( $\times 1.17$ )	0.13	-0.114 ( $\times 0.77$ )	0.33	+0.0458	$< 10^{-4}$
SWAG ViT-L/16	+0.104	$< 10^{-4}$	+0.012 ( $\times 1.03$ )	0.28	-0.185 ( $\times 0.65$ )	0.96	+0.0429	$< 10^{-4}$
SimCLR R50x4	+0.080	0.007	+0.031 ( $\times 1.08$ )	0.32	-0.088 ( $\times 0.82$ )	0.53	+0.0322	0.15
BiT-M R152x2	+0.048	0.045	+0.167 ( $\times 1.47$ )	$< 10^{-4}$	+0.119 ( $\times 1.32$ )	0.021	+0.0191	0.041
CLIP	+0.025	0.11	+0.140 ( $\times 1.38$ )	$< 10^{-4}$	+0.280 ( $\times 1.91$ )	$< 10^{-4}$	+0.0131	0.31
BiT-M R152x4	+0.051	0.13	+0.126 ( $\times 1.34$ )	0.008	+0.083 ( $\times 1.21$ )	0.015	+0.0130	0.18
ResNet50 (SIN)	+0.013	0.30	+0.141 ( $\times 1.38$ )	$< 10^{-4}$	+0.196 ( $\times 1.57$ )	$< 10^{-4}$	+0.0157	0.96
ResNet50 (SIN+IN)	-0.008	0.37	+0.225 ( $\times 1.68$ )	$< 10^{-4}$	+0.479 ( $\times 3.01$ )	$< 10^{-4}$	+0.0023	0.38
ResNeXt101 (SWSL)	+0.013	0.64	+0.100 ( $\times 1.26$ )	0.002	+0.244 ( $\times 1.75$ )	$< 10^{-4}$	+0.0084	0.96
SimCLR R50x1	+0.011	0.64	+0.203 ( $\times 1.59$ )	$< 10^{-4}$	+0.370 ( $\times 2.34$ )	$< 10^{-4}$	+0.0229	0.58
MoCoV2	+0.005	0.67	+0.112 ( $\times 1.29$ )	0.005	+0.316 ( $\times 2.07$ )	$< 10^{-4}$	+0.0142	0.96
InfoMin	+0.001	0.72	+0.123 ( $\times 1.33$ )	0.004	+0.275 ( $\times 1.88$ )	$< 10^{-4}$	+0.0076	0.83

**Panel B: Fixed-effects regressions testing whether RD parameters add information beyond accuracy.**

Predictor	$\hat{\beta}$ (SE)	$p_{\beta}$	$\hat{\kappa}$ (SE)	$p_{\kappa}$
Accuracy (within-block)	-0.516 (0.080)	$< 10^{-4}$	-3.286 (0.174)	$< 10^{-4}$
LargeCNNs	+0.186 (0.050)	$2.01 \times 10^{-4}$	+0.590 (0.109)	$< 10^{-4}$
VisionTransformers	+0.144 (0.047)	0.002	+0.711 (0.103)	$< 10^{-4}$
SemiSupervised	+0.163 (0.050)	0.001	+0.748 (0.109)	$< 10^{-4}$
SelfSupervised	+0.106 (0.046)	0.021	+0.615 (0.099)	$< 10^{-4}$
ShapeBiased	+0.196 (0.050)	$< 10^{-4}$	+0.619 (0.109)	$< 10^{-4}$
LocalModels	+0.228 (0.053)	$< 10^{-4}$	+0.765 (0.116)	$< 10^{-4}$

**Notes.** A block is a matched experimental context (experiment  $\times$  perturbation condition). All paired tests compare models to humans *within the same block*. In Panel A,  $\Delta$  denotes the within-block median difference (model – humans) and “fold” is  $10^{\Delta}$  for log-parameters. In Panel B, humans are the reference family. Block fixed-effects absorb all block-specific shifts (coefficients omitted for brevity). Reported  $p$ -values are two-sided.

### Rate-Distortion Signatures of Generalization and Information Trade-offs

**Table 3. Model-/regime-level paired comparisons vs humans across matched perturbation blocks.** For each model/regime, we compute within-block differences relative to humans (model – humans) across matched contexts (*blocks*, Experiment  $\times$  condition), then test whether the median within-block difference differs from zero using two-sided Wilcoxon signed-rank tests. We report the block count ( $n_{\text{blocks}}$ ), median within-block difference ( $\Delta$ ), rank-biserial effect size ( $r_{\text{rb}}$ ), and BH–FDR-adjusted  $q$  within each metric (across the 6 model contrasts). For log-parameters,  $\Delta\beta$  and  $\Delta\kappa$  are in  $\log_{10}$  units (fold-change =  $10^\Delta$ ).

Model / regime	$n_{\text{blocks}}$	Accuracy			$\beta$ ( $\log_{10}$ )			$\kappa$ ( $\log_{10}$ )			AUC		
		$\Delta\text{Acc}$	$q_{\text{Acc}}$	$r_{\text{rb}}$	$\Delta\beta$	$q_\beta$	$r_{\text{rb}}$	$\Delta\kappa$	$q_\kappa$	$r_{\text{rb}}$	$\Delta\text{AUC}$	$q_{\text{AUC}}$	$r_{\text{rb}}$
All-noise	33	+0.177	$3.52 \times 10^{-6}$	+0.996	+0.0408	$8.88 \times 10^{-2}$	+0.358	-0.145	$4.23 \times 10^{-4}$	-0.715	+0.0112	$7.93 \times 10^{-3}$	+0.544
Specialised	33	+0.120	$3.52 \times 10^{-6}$	+0.971	+0.0913	$1.08 \times 10^{-1}$	+0.323	-0.177	$3.20 \times 10^{-3}$	-0.590	+0.00471	$4.35 \times 10^{-2}$	+0.405
VGG-19	81	-0.0162	$3.77 \times 10^{-3}$	-0.398	+0.292	$3.64 \times 10^{-9}$	+0.778	+0.368	$3.50 \times 10^{-11}$	+0.881	-0.0209	$2.83 \times 10^{-7}$	-0.699
Finetuned	35	-0.0798	$6.07 \times 10^{-3}$	-0.559	+0.188	$1.31 \times 10^{-5}$	+0.863	+0.253	$9.98 \times 10^{-5}$	+0.775	-0.0256	$2.57 \times 10^{-5}$	-0.835
ResNet-152	81	-0.0104	$5.15 \times 10^{-2}$	-0.259	+0.292	$4.46 \times 10^{-10}$	+0.833	+0.335	$1.47 \times 10^{-9}$	+0.792	-0.0197	$1.72 \times 10^{-5}$	-0.569
GoogLeNet	81	-0.000154	$8.32 \times 10^{-2}$	-0.222	+0.299	$1.80 \times 10^{-8}$	+0.736	+0.331	$1.47 \times 10^{-9}$	+0.788	-0.0222	$1.02 \times 10^{-6}$	-0.653

**Notes.** A *block* is an (experiment  $\times$  condition) context. All comparisons are paired to humans *within the same block*. Reported  $\Delta$  values are blockwise medians of (model – humans).  $q$  values are BH–FDR adjusted *within each metric* across the six model contrasts. *Finetuned* comprises 20 independently trained instances. Blockwise finetuned summaries are aggregated across instances before block-collapsed testing, and overlap with humans is  $n_{\text{blocks}} = 35$ .